

# Engineering 2D square lattice Hubbard models in 90° twisted Ge/SnX (X=S, Se) moiré superlattices

Qiaoling Xu,<sup>1,2</sup> Nicolas Tancogne-Dejean,<sup>3</sup> Emil Viñas Boström,<sup>3</sup> Dante M. Kennes,<sup>4,3,\*</sup> Martin Claassen,<sup>5,†</sup> Angel Rubio,<sup>3,6</sup> and Lede Xian<sup>2,3,‡</sup>

<sup>1</sup>College of Physics and Electronic Engineering, Center for Computational Sciences, Sichuan Normal University, Chengdu 610068, China

<sup>2</sup>Songshan Lake Materials Laboratory, 523808 Dongguan, Guangdong, China

<sup>3</sup>Max Planck Institute for the Structure and Dynamics of Matter, Luruper Chaussee 149, 22761 Hamburg, Germany

<sup>4</sup>Institut für Theorie der Statistischen Physik, RWTH Aachen University and

JARA-Fundamentals of Future Information Technology, 52056 Aachen, Germany

<sup>5</sup>Department of Physics and Astronomy, University of Pennsylvania, Philadelphia, PA 19104

<sup>6</sup>Center for Computational Quantum Physics, Simons Foundation Flatiron Institute, New York, NY 10010 USA

(Dated: June 11, 2024)

Due to the large-period superlattices emerging in moiré two-dimensional (2D) materials, electronic states in such systems exhibit low energy flat bands that can be used to simulate strongly correlated physics in a highly tunable setup. While many investigations have thus far focused on moiré flat bands and emergent correlated electron physics in triangular, honeycomb and quasi-one-dimensional lattices, tunable moiré realizations of square lattices subject to strong correlations remain elusive. Here we propose a feasible scheme to construct moiré square lattice systems by twisting two or more layers of 2D materials in a rectangular lattice by 90 degrees. We demonstrate such scheme with twisted GeX/SnX (X=S,Se) moiré superlattices and calculate their electronic structures from first principles. We show that the lowest conduction flat band in these systems can be described by a square lattice Hubbard model with parameters which can be controlled by varying the choice of host materials, number of layers, and external electric fields. In particular, twisted double bilayer GeSe realizes a square lattice Hubbard model with strong frustration due to the next nearest neighbour hopping that could host unconventional superconductivity, in close analogy to the Hubbard model for copper-oxygen planes of cuprate high-temperature superconductors. The presented scheme uses 90-degree twisted 2D materials with rectangular unit cells as a generic platform for realizing square lattice Hubbard models, establishing a new route for studying its rich phase diagram of magnetism, charge order, and unconventional superconductivity in a highly tunable setting.

## I. INTRODUCTION

The electronic Hubbard model [1–3] is ubiquitous in condensed matter research. In its original form it contains only two parameters: the electron hopping amplitude between adjacent sites ( $t$ ) and a strong on-site interaction ( $U$ ) between electrons of opposite spin. Despite its simplicity, the Hubbard model was employed early on to describe interaction-driven Mott metal-insulator transitions, with rich possibilities for magnetic order or quantum spin liquids at low temperatures [4, 5]. Upon doping, the single band electronic Hubbard model is purported to support high-temperature superconductivity [6] and charge density waves [7, 8], while strange metallicity and the pseudogap regime at finite temperatures have attracted considerable attention [9–11].

From a theoretical perspective the apparent simplicity, yet intrinsic complexity, of the Hubbard model has captured the imagination of generations [12–14]. For many state-of-the-art methods of quantum many-body physics the (approximate) solution of the Hubbard model is viewed as an essential benchmark. Many complementary theoretical advances [7, 11, 15], such as dynamical mean-field theory, quantum Monte-Carlo, renormalization group based approaches or tensor network ansätze try to draw a picture as complete as pos-

sible for the different regimes of their validity. For example, one-dimensional Hubbard models are often amendable to tensor networks [16, 17] while high-dimensional Hubbard models can be well described by a dynamical mean field approach [18]. The most pertinent case of the two-dimensional fermionic Hubbard model can be addressed on bipartite lattices and at half filling using a quantum Monte Carlo description [19–22], but the superconducting state emerging at finite doping and frustration is difficult to capture with (numerically) exact methods beyond quasi-one-dimensional ladder geometries [23].

An alternative approach which has gained tremendous attention recently is to turn the problem upside-down from computation to (quantum) simulation: Instead of a theoretical approach or classical computation, cold gases or other platforms can provide highly controllable experimental simulations of the model system [24–31]. Here, the simulation of the (fermionic or bosonic) Hubbard model again constitutes one of the main goals and benchmarks. Much progress has been achieved concerning quantum magnetism in Hubbard-type models utilizing such a simulation approach, but yet many questions – e.g. the one of unconventional superconductivity – remain beyond the current simulation capabilities due to the ultralow temperatures that are necessary to access the corresponding energy scales [32].

With the recent rise of ultra-clean and highly controllable two-dimensional materials, a new protagonist has entered the stage [33–37]. These materials are unique as they provide a high degree of tunability via heterostructure stacking, gating, and stress or strain, in a low disorder setting. Using stack-

\* Email: Dante.Kennes@rwth-aachen.de

† Email: claassen@sas.upenn.edu

‡ Email: xianlede@ssl.org.cn

ing configurations that include either a relative twist between adjacent layers or an intrinsic lattice constant mismatch between layers of different materials, such moiré heterostructures have recently become one of the main research focus of the field [38–48]. The large scale moiré interference pattern emerging at low twist angle or small lattice constant mismatches allows to quench the kinetic energy scales promoting competing energy scales (such as the potential, spin-orbit or phononic couplings). This concept has been explored extensively mainly in graphitic or transition metal chalcogenide materials and has raised the hope to realize many of the prototypical models of condensed matter physics [49–57]. In this work we propose moiré materials engineering as an inroad to realize the prototypical square lattice Hubbard model with a nearest neighbor hopping  $t$  and next nearest neighbor hopping  $t'$ . In contrast to the usual paradigm of using small twist angles we study a bilayer system with each layer exhibiting a rectangular but only slightly non-square unit cell rotated by  $90^\circ$  with respect to each other. The small lattice constant mismatch of the two sides of the rectangular unit cell combined with the rotation naturally generates a moiré pattern giving rise to the square lattice structure. This provides a pivotal materials-based platform to study unconventional superconductivity in a highly controlled two-dimensional materials platform allowing to bridge the gap left open between theoretical approaches and quantum simulations in the future.

## II. MOIRÉ SQUARE SUPERLATTICES FROM TWISTED RECTANGULAR LATTICES

### A. General strategy

The natural way to obtain a 2D moiré square lattice is through twisting two layers of 2D materials with a square lattice unit cell. However, in practice, the number of 2D layered materials with square lattices that can be synthesized or exfoliated down to monolayer or few layers in experiments is very limited. On the other hand, thin layers of 2D materials with rectangular lattices are more commonly studied, such as the group-IV monochalcogenides  $\text{GeX/SnX}$  ( $X=\text{S, Se, Te}$ ) family [58] and  $\text{PdSe}_2$  [59]. Herein, we propose a general strategy to construct moiré square lattices basing on the orthorhombic van der Waals (vdW) crystal structures with rectangular unit cell, as shown in Figure 1.

Starting with two identical layers of 2D materials in a simple rectangular lattice with lattice constants  $a \neq b$ , one can twist one of the layers by  $90^\circ$  and stack it on top of the other layer. In this way, the lattice constants of the top and the bottom layers along the same axis are no longer equal and a moiré pattern will emerge. In the real space, the moiré wavelength  $L$  along the x and the y axis are both determined by the lattice mismatch between the original lattice constants  $a$  and  $b$ , i.e.,  $L_x = L_y = ma = nb$  (see Figure 1). Therefore, the moiré period along the x and the y axis are equal and the resultant moiré pattern becomes a square lattice. In reciprocal space, as shown in Figure 1(c), the reciprocal lattice vectors of the top/bottom layer and those of the moiré superlattice are con-

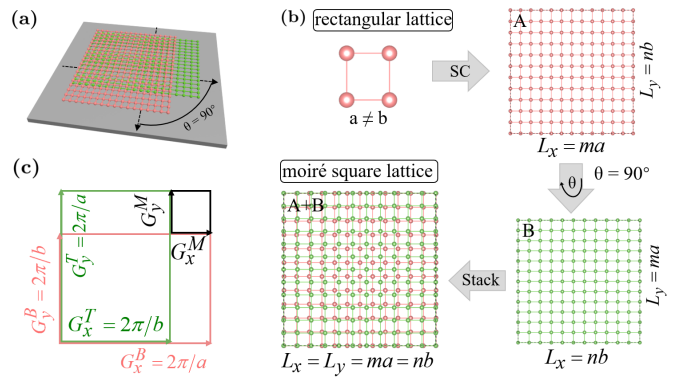


FIG. 1. **General strategy of constructing moiré square lattices.** (a) Schematic illustration of the  $90^\circ$  twisted 2D layers. (b) Flow chart of the construction of the moiré square superlattice using 2D layers of rectangular lattices with lattice constants  $a$  and  $b$  with  $a \neq b$ . (c) Brillouin zone of the  $90^\circ$  twisted rectangular lattices.

nected by the following relation:

$$G_x^B - G_x^T = G_x^M, \quad (1)$$

where  $G_x^B = 2\pi/a$ ,  $G_x^T = 2\pi/b$  and  $G_x^M = 2\pi/L$  are the reciprocal lattice vectors of the bottom layer, the top layer and the moiré superlattice, respectively. Thus, real space lattice vectors  $a$ ,  $b$  and  $L$  satisfy the following equation:

$$\frac{1}{a} - \frac{1}{b} = \frac{1}{L}. \quad (2)$$

So  $L$  can be determined by the expression  $L = [(1/a) - (1/b)]^{-1}$ . The smaller the difference between the original lattice constants  $a$  and  $b$ , the larger the moiré period  $L$ . In practice, we will need to slightly strain the original lattice constants  $a$  and  $b$  such that we can construct a commensurate supercell containing only one moiré wavelength (see the Table I). This method of straining lattice constants to achieve commensurability was also very successful in the past to construct moiré triangular lattices using lattice mismatches of TMD heterostructures [44, 51, 60, 61].

### B. $90^\circ$ twisted bilayer $\text{GeX/SnX}$ ( $X=\text{S, Se}$ )

We first apply this strategy to construct moiré square superlattices with 2D  $\text{GeSe}$  that has a rectangular lattice structure similar to that of black phosphorene [62]. The optimized atomic structures of  $90^\circ$  twisted bilayer  $\text{GeSe}$  is shown in Figure 2. As expected, the twisted structure exhibits a moiré square superlattice with moiré lattice constant of  $25.658 \text{ \AA}$ . The detailed structural parameters are summarized in Table I. The moiré structure mainly consists of two types of AA-like and two types of AB-like local stacking registries called  $\text{AA}^\alpha$ ,  $\text{AA}^\beta$ ,  $\text{AB}^\alpha$  and  $\text{AB}^\beta$ . Each of these is uniquely identified by which atoms fall on top of each other in a top and side view as categorized in the right panels of Figure 2. These four special stackings can be transformed into each other by translational

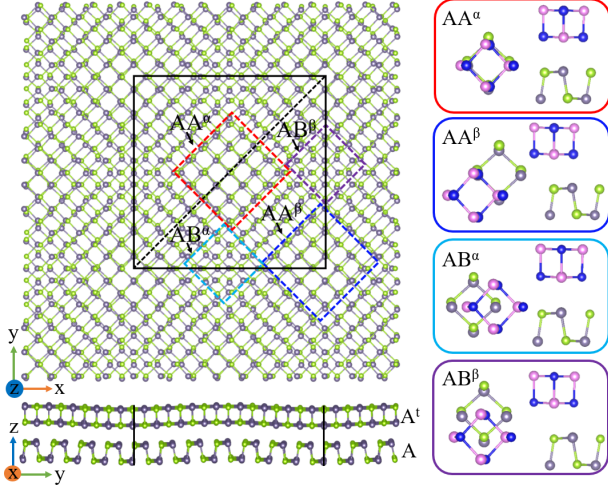


FIG. 2. **Moiré structure of 90° twisted bilayer GeSe.** The top and the side views of the atomic structure are shown in upper left and lower left panels, respectively.  $A^t$  in the side view is used to indicate the layer twisted by 90° with respect to the layer labeled as A. The moiré unit cell is indicated by black solid lines. The black dashed line represents the in-plane C2 rotational axis. The top and the side views of the atomic structures of the local stackings of  $AA^\alpha$ ,  $AA^\beta$ ,  $AB^\alpha$ , and  $AB^\beta$  are shown in right panels. The Ge and the Se atoms are represented by green/blue and grey/pink balls, respectively.

sliding of one of the basal planes in the unit cell. Moreover, for such twisted bilayer structures, not only are the lattice constants along the two orthogonal directions equal, but the system also has an in-plane C2 rotational symmetry along the diagonal direction of the moiré cell (see Figure 2 dotted line), leading to equivalent electronic properties along the x and the y directions.

We then calculate the electronic band structures for a 90° twisted bilayer GeSe system using density functional theory (DFT) calculations. The result is shown in Figure 3(a). As expected, the band structure of the system along the X and the Y directions are identical. Due to the moiré modulation, an isolated flat band with ultra-small bandwidth of 1.5 meV emerges at the conduction-band edges (CBE). The calculated charge density distribution of the flat band shows that these electronic states are localized at the  $AA^\alpha$  regions, forming a square checkerboard pattern in real space (see Figure 3(d)). Based on these results, we model the flat band with an effective tight-binding (TB) model on a square lattice for which the Hamiltonian can be written as:

$$\mathbf{H} = -t \sum_{\langle i,j \rangle, \sigma} c_{i\sigma}^\dagger c_{j\sigma} + t' \sum_{\langle\langle i,j \rangle\rangle} c_{i\sigma}^\dagger c_{j\sigma}, \quad (3)$$

where  $t$  and  $t'$  are the nearest-neighbour and the next-nearest-neighbour hopping amplitudes, respectively;  $\langle \dots \rangle$  and  $\langle\langle \dots \rangle\rangle$  represent the summation over the nearest-neighbours and next-nearest-neighbours, respectively;  $c_{i\sigma}$  ( $c_{i\sigma}^\dagger$ ) annihilates (creates) an electron at site  $i$  with spin  $\sigma = \uparrow, \downarrow$ . As the spin-orbit coupling for the flat band is negligible and thus the spins can be regarded as degenerate, using the notations shown in

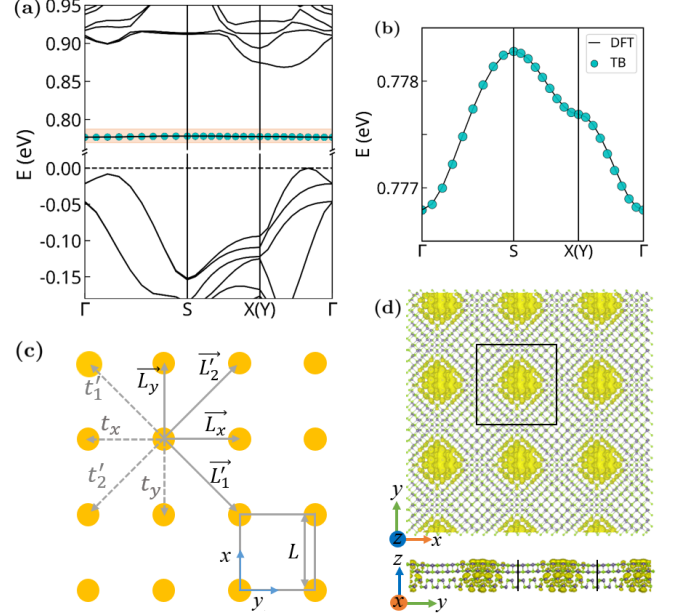


FIG. 3. **Moiré flat bands of 90° twisted bilayer GeSe.** (a) Low-energy band structure near the band edge. The dashed line indicates the Fermi level. (b) The enlarged band structure corresponding to the shaded region in (a), which shows the dispersion of the moiré flat band at the CBE. The black solid line and the cyan dots denote the results calculated with DFT and the effective TB model, respectively. (c) Schematic diagram of the square lattice effective TB model. (d) Top view (upper panel) and side view (lower panel) of partial charge density distribution in real space for the flat-band state at the CBE.

TABLE I. **Parameters of constructing square lattices for 90° twisted bilayer GeX/SnX.**

| Materials | Unit cell (a, b)/Å | (m, n)   | (m', n')  | Scale (p, q)/% |
|-----------|--------------------|----------|-----------|----------------|
| GeS       | (3.64, 4.29)       | (7, 6)   | (6, -7)   | (0.5, -0.5)    |
| GeSe      | (3.83, 4.38)       | (8, 7)   | (7, -8)   | (0.08, -0.08)  |
| SnS       | (3.98, 4.33)       | (12, 11) | (11, -12) | (-0.2, 0.2)    |

Figure 3(c), the dispersion relation for one of the spin component can be written as:

$$E(k) = 2t_x \cos k_x L + 2t_y \cos k_y L + 2t'_1 \cos(k_x L + k_y L) + 2t'_2 \cos(k_x L - k_y L), \quad (4)$$

where  $t_x(t_y)$  denotes the nearest-neighbour hopping amplitude along the  $x(y)$  direction and  $t'_1/t'_2$  the next-nearest-neighbour hoppings along the diagonal directions;  $L$  denotes the lattice constant for the moiré square superlattice. As shown in Figure 3(b), the fitted effective TB model gives almost identical band dispersion as the one calculated with DFT for the flat band at the CBE in the 90° twisted bilayer GeSe with  $t_x = t_y$  and  $t'_1 = t'_2$  (see Table II for values of the fitted parameters). The next nearest neighbour hopping versus nearest neighbour hopping ratio  $t'_1/t_x$  equals 10.32% for this system.

We further apply the strategy to other 2D group-IV monochalcogenides GeS and SnS bilayer. Although the lattice

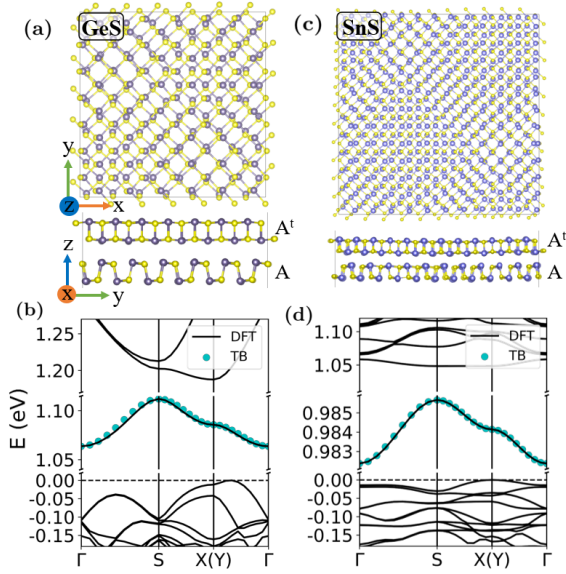


FIG. 4. **Moiré flat bands of  $90^\circ$  twisted bilayer GeS and SnS.** The atomic and the electronic structures of  $90^\circ$  twisted bilayer GeS (a, b) and SnS (c, d). The low energy flat bands at the CBE are fitted well by the effective TB model.

constants of GeS and SnS are different from those of GeSe, the generality of the strategy ensures that the moiré structures end up as square superlattices. The atomic structures of the  $90^\circ$  twisted bilayer GeS and SnS are shown in Figures 4(a) and 4(c) and the detail parameters are listed in Table I. The moiré patterns of these systems are mainly formed by four local stacking domains similar to those of twisted bilayer GeSe. The corresponding DFT band structures are shown in Figures 4(b) and 4(d). Similar to twisted GeSe, a flat bands with narrow bandwidths of 48 meV and 3 meV appear at the CBE for twisted bilayer GeS and SnS, respectively. As shown in Figure 4, these flat bands can be accurately fit by the effective square lattice model described by Equation (4) and the detail fitted parameters are shown in Table II.

### C. $90^\circ$ twisted multilayer GeX/SnX (X=S, Se)

The general strategy we proposed can also be applied to twisted multilayer GeX/SnX (X=S, Se). With the additional layer degree of freedom, we can further engineer different flat band dispersion in a moiré square lattice. Taking the GeSe structures as typical examples, the multilayer moiré square superlattices can be generated by twisting monolayer on pristine bilayer (I-II), on pristine trilayer (I-III) or bilayer on bilayer (II-II) as shown in Figures 5(a-c). The untwisted layers remain in their natural AB stacking in their pristine bulk form. The corresponding band structures for these moiré superlattices are given in Figures 5(d-f). Similar to the twisted bilayer systems, all of these twisted multilayer structures exhibit very flat minibands appearing at the CBE with bandwidths of 4 meV, 7 meV and 1.4 meV, respectively. In these three types of

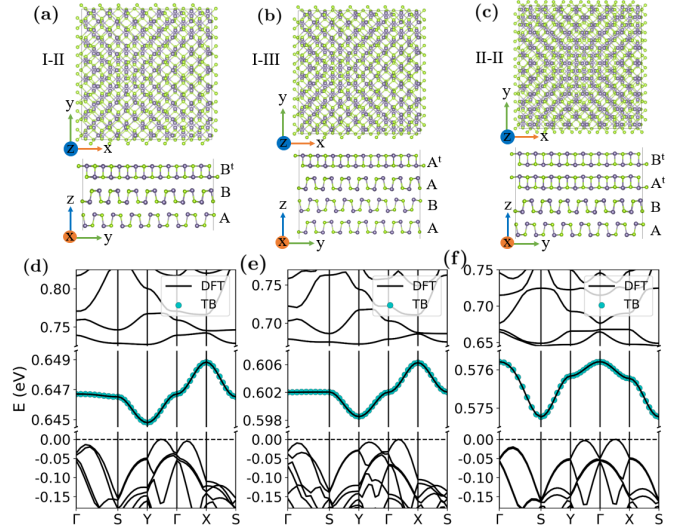


FIG. 5. **Moiré flat bands of  $90^\circ$  twisted multilayer GeSe.** (a-c) Top (upper panel) and side views (lower panel) of the atomic structures for the  $90^\circ$  twisted monolayer-bilayer (I-II), monolayer-trilayer (I-III) and AB-A'B' type of bilayer-bilayer (II-II) configurations, where AB, A' and B' indicate natural bilayer from bulk,  $90^\circ$  twisted A layer and  $90^\circ$  twisted B layer, respectively. The grey and green balls represent Ge and Se atoms, respectively. (d-f) The corresponding low energy band structures with fitting by the effective TB model.

twisted multilayer structures, the in-plane  $C_2$  rotational symmetry is broken and the electronic properties along the  $x$  and the  $y$  axis are not equivalent. Nevertheless, the bottom moiré flat bands at the CBE in the twisted multilayer superlattices can also be described by the simple square lattice effective model given by Equation (4) with different values for  $t_x$  and  $t_y$  (see fitted parameters in Table II). Therefore, with ultraflat bands and inequivalent hoppings along the  $x$  and the  $y$  axis, these moiré systems can be used to realize anisotropic square lattice Hubbard models.

For twisted multilayer systems with even number of layers, the in-plane  $C_2$  rotational symmetry can be restored by designing the twist stacking. For example, in the twisted double bilayer system, by twisting the top two layers by  $90^\circ$  with respect to the bottom two layers, one can obtain a moiré square superlattice in the AB-A'B' type of stacking (Figure 5(c)). By further flipping the top two layers up side down in the AB-A'B' type of twisted double bilayer superlattice, one obtains the AB-B'A' type of moiré superlattice (Figure 6(a)). While the in-plane  $C_2$  rotational symmetry along the diagonal direction of the supercell is absent in the AB-A'B' type of moiré superlattice, it is restored in the the AB-B'A' type. As shown in Figure 6(b), the band dispersion for the AB-B'A' type twisted double bilayer GeSe along the  $x$  and the  $y$  directions are exactly the same due the symmetry in the system. In particular, the lowest moiré flat band at the CBE can be fitted to the effective TB model with  $t_x = t_y$  (see Table II). Interestingly, for twisted multilayer moiré square superlattices, the next nearest neighbour hopping versus nearest neighbour hopping ratio  $t'/t$  is generally larger than that of the twisted bilayer. For the



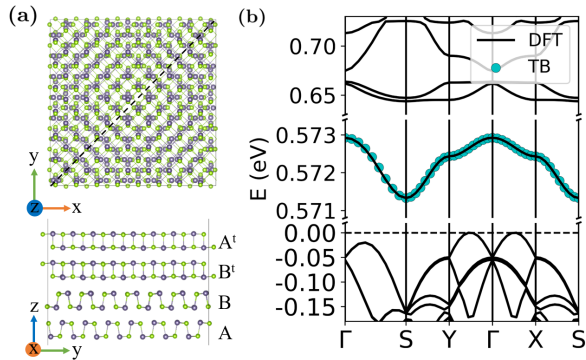


FIG. 6. **90° twisted double bilayer GeSe with symmetry.** The atomic (a) and electronic structure (b) of the AB-B'A' type of twisted double bilayer GeSe where the C2 symmetry around the diagonal axis of the moiré supercell is preserved. The low-energy flat band at CBE is fitted by the effective TB model shown in green markers.

AB-B'A' type twisted double bilayer GeSe, this value reaches  $\sim 19\%$ .

#### D. Correlation properties of 90° twisted GeX/SnX (X=S, Se) moiré superlattices

In flat bands, electronic interactions can dictate electronic properties and give rise to emergent phases in a highly-tunable setting. In order to gain insight in the role of electronic correlations, we complemented our DFT simulations by DFT+ $U$ + $V$  simulations, in which an on-site effective Hubbard  $U$  and an intersite interaction  $V$  (for the localized Wannier orbitals constructed from the DFT flat bands) are added to the DFT Hamiltonian. These effective electronic parameters are evaluated *ab initio* (see the Appendix for more details) in order to determine the ground state of the system when static correlation effects are included. To this end, we performed several DFT+ $U$ + $V$  calculations at half filling of the flat band in the unit cell of twisted GeSe, as well as in doubled  $2 \times 1$  supercells, in order to determine the lowest-energy configuration and allow for collinear and Néel antiferromagnetic order. As expected for a square-lattice Hubbard model with weak frustration, we found that the system exhibits an antiferromagnetic instability at half filling [63], with the Néel antiferromagnetic order been lower than the collinear antiferromagnetic order. However, in contrast to conventional antiferromagnetic insulators composed of atomic orbitals, the effective magnetic moments extend over the charge accumulation regions in the moiré unit cell. Each localized Wannier state is found to host a finite magnetization. The Wannier states obtained at the DFT level for the  $2 \times 1$  supercell with Néel antiferromagnetic order of GeSe are shown in Figure 7(a) and 7(b) and the corresponding magnetization, obtained once on-site and intersite interactions are included is shown in Figure 7(c). The obtained effective electronic parameters give an on-site interaction  $U_{\text{eff}} \approx 1.45\text{meV}$ , corresponding to  $U/t \simeq 7.8$ , and a ratio of the intersite interaction to the on-site effective one

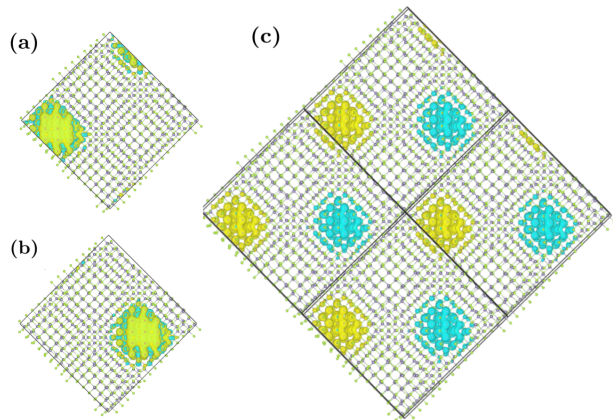


FIG. 7. **Electronic ground states of the moiré flat bands in the 90° twisted bilayer GeSe with correlations.** (a-b) Wannier states corresponding to the two flat bands of a checkerboard  $2 \times 1$  supercell of twisted bilayer GeSe. (c) The corresponding magnetization density obtained from DFT+ $U$ + $V$  at half-filling.

to be  $U_{\text{eff}}/V \approx 10$ .

Having established a tunable moiré realization of a square-lattice Hubbard antiferromagnet at half filling, gate-induced doping, variations of the twist angle and materials compositions now open up new routes for testing longstanding questions regarding the phase diagram of square lattice Hubbard models, mechanisms for unconventional superconductivity, intertwined charge orders and the role of frustration [11, 12, 14]. For strong interactions, prior theoretical studies indicate a close competition between charge/spin stripe order and a uniform  $d$ -wave superconducting phase, which give way to a Fermi liquid at dilute filling [14]. However, more exotic states such as pair-density wave order have been proposed as well [11, 64–66]. Of the materials parameterized in Table II, four-layer twisted GeSe configurations most closely mirror weak frustration  $|t'/t| \approx 0.2$  representative of cuprate high-temperature superconductors [13, 23]. In contrast to cuprates, electron and hole doping away from half filling are flipped by virtue of  $t'$  and  $t$  carrying the same sign. Interestingly, the proposed moiré realization of a two-dimensional Hubbard model can serve as a simulator to explore competing ground states at finite filling. For instance, while the unfrustrated Hubbard model at 1/8 doping was found by multiple methods to favor a period-8 stripe phase without superconductivity [7, 8], the stability of stripe order, variations of its period, and the onset of  $d$ -wave superconductivity for variations of either filling or frustration has attracted much attention [8, 67–70]. Moiré square lattice systems can simulate the resulting phase diagram by changing the layer composition.

#### E. Tuning via external electric fields

Electric fields have been demonstrated to be an efficient strategy to tune moiré flat bands in other moiré materials.

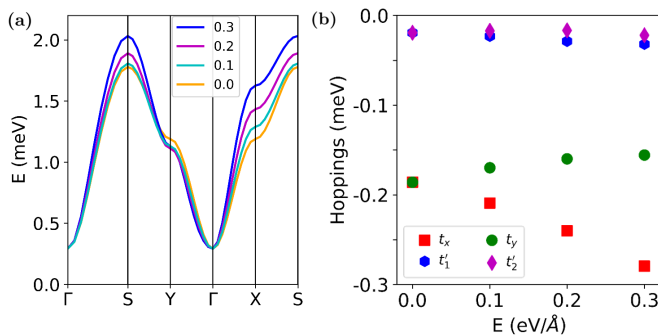


FIG. 8. **Electric field tuning of moiré flat bands in 90° twisted bilayer GeSe.** (a) The flat bands at the CBE under various vertical electric field ( $E$ ) with the value of 0.0, 0.1, 0.2 and 0.3 eV/Å. (b) The effective model fitting parameters as a function of the electric field.

Therefore, we also investigate the flat bands in 90° twisted bilayer GeSe subjected to an external electric field applied perpendicularly to the layers. Figure 8(a) shows the low-energy flat band structures of the CBE under four different strengths of external electric fields with the value of 0.0, 0.1, 0.2 and 0.3 eV/Å. By comparing these structures, we find that the electric field has a greater impact on the band dispersion curves in the high symmetry k-points Y and X, while it has a negligible effect on the energy scale of the total bandwidth. When no electric field is applied, the energy positions at the X and Y point are the same. As the electric field increase, the energy difference at the X and Y point will become larger. We also use TB fits to describe the influence of electric fields. Figure 8(b) depicts the effective model fitting parameters given as a function of electric fields. It indicates a wide range of tunability for hopping terms, especially for the hoppings  $t_x$  and  $t_y$ , compared to the zero electric field case.

### III. CONCLUSIONS

Our work proposes a general scheme to use rectangular-lattice 2D van der Waals materials to construct moiré square superlattices. We predict that moiré heterostructures of 90° twisted bilayers and multilayers of the rectangular-lattice transition-metal dichalcogenide family (Ge/Sn)(S/Se) can provide a platform to realize the paradigmatic square-lattice Hubbard model with repulsive interactions in a tunable setting. In this set of compounds, layer composition grants a twofold handle to tune electronic frustration and drive the material into a regime with narrow square-lattice moiré bands dominated by strong Coulomb interactions. Focusing on 90° rotated bilayers of GeSe, we computed the strength of Coulomb interactions and predict the formation of a paradigmatic square-lattice Mott insulator with Néel order at half filling. Combined with gate-tunable carrier doping, this suggests that 90°-twisted (Ge/Sn)(S/Se) can serve as an experimental solid-state platform to simulate the phase diagram of the copper-oxygen planes of cuprate high-temperature superconductors, to provide new experimental insight into the nature of

the pseudogap, the role of electronic frustration, and competing and intertwined superconducting and density wave orders.

### ACKNOWLEDGMENTS

L.X. and Q.X. acknowledge the support by the National Key Research and Development Program of China (Grant No. 2022YFA1403501), Guangdong Basic and Applied Basic Research Foundation (Grant No. 2022B1515120020), the Hefei National Research Center for Physical Sciences at the Microscale (KF2021003), and the Max Planck Partner group programme. D.M.K acknowledge funding by the Deutsche Forschungsgemeinschaft (DFG, German Research Foundation) within the Priority Program SPP 2244 “2DMP” - 443274199 and under Germany’s Excellence Strategy - Cluster of Excellence Matter and Light for Quantum Computing (ML4Q) EXC 2004/1 - 390534769. M.C. acknowledges support by the U.S. Department of Energy (DOE), Office of Basic Energy Sciences, under Award No. DE-SC0024494. We acknowledge computational resources provided by RWTH Aachen University under project number rwth0763. This work was supported by the Max Planck-New York City Center for Nonequilibrium Quantum Phenomena. This work was supported by the European Research Council (ERC-2015-AdG694097), the Cluster of Excellence ‘Advanced Imaging of Matter’ (AIM), Grupos Consolidados (IT1249-19) and Deutsche Forschungsgemeinschaft (DFG) -SFB-925–project 170620586.

### Appendix A: MODEL AND COMPUTATIONAL APPROACHES

*Density functional theory calculations* —The present calculations are done within the framework of density functional theory (DFT) using the plane-wave pseudopotential approach performed in the VASP code [71]. The electron-ion interactions can be described by the projector augmented wave (PAW) pseudopotentials [72]. Configurations of  $4s^24p^2$  for Ge,  $5s^25p^2$  for Sn,  $3s^23p^4$  for S and  $4s^24p^4$  for Se are considered as valence electrons. We use the Perdew-Burke-Ernzerhof (PBE) parameterization of the generalized gradient approximation [73] as the exchange correlation functional. We calculate the equilibrium lattice parameters of GeS in the bulk phase and found that the DFT-TS vdW functionals [74] provide better agreement with the experimental values [62] within less than 1% errors. The DFT-TS vdW functional is then adopted for all calculations. A plane-wave basis set with an energy cutoff of 400 eV and a  $1 \times 1 \times 1$  momentum grid are used to characterize the ground state and the mechanical relaxation. Our calculations are fully relaxed (w.r.t. all the atoms), which is known to be important in other moiré systems to avoid artificial effects stemming from unrelaxed structures. The relaxation procedure ensures that the force on each atom converges to values smaller than 0.01 eV/Å. A long z-direction auxiliary vacuum region larger than 15 Å is added to avoid the artificial interaction between the periodic slabs. As

spin-orbit coupling (SOC) is found to have negligible effects on the flat bands calculated for the systems, we exclude SOC in the calculations.

*DFT+U+V calculations* — The *ab initio* evaluation of the effective electronic parameters (on-site effective Hubbard  $U_{\text{eff}} = U - J$  and the intersite interaction  $V$ ) and the DFT+U+V calculations are performed using the Octopus code [75, 76]. A real-space spacing of 0.4 Bohr is chosen, and we employ HGH norm-conserving pseudopotentials [77]. The LDA is used for describing the local DFT part. The vacuum size, atomic coordinates and lattice constant are taken to be the same as for the DFT treatment, as described above. In order to analyse if the system present or not an antiferromagnetic instability when correlations are taken into account, we constructed a doubled-cell by repeating the DFT unit cell along the  $x$ -axis. We employed a  $3 \times 3$  k-point grid for the unit cell and the  $1 \times 1$  k-point grid for the double cells. The localized subspace was constructed using the Wannier90 library [78], taking the flat bands obtained from the LDA calculation performed with the Octopus code. We then populated these bands at half filling by adding an excess charge of two electrons in the system and performed DFT+U+V calculations. We performed non-polarized and spin-polarized calculations for the unit cell, as well as a spin-polarized calculations for the double cells. In all spin-polarized calculations, we started from random magnetic configurations in order to determine the ground-state of the system. Only the first nearest neighbor interaction was considered in the intersite interaction.

The standard approach to estimate the on-site  $U$  and intersite  $V$  rely on the cRPA method. This method is however prohibitively expensive for been applied to twisted bilayer systems, and an alternative approach needs to be employed. In order to get a first estimate on the relative strength of the on-site and intersite interaction, we compute first the Coulomb integrals of the bare Coulomb potential.

$$\langle \phi_m^I \phi_m^I | v | \phi_{m'}^J \phi_{m'}^J \rangle = \int d\mathbf{r} d\mathbf{r}' |\phi_m(\mathbf{r})|^2 \frac{1}{|\mathbf{r} - \mathbf{r}'|} |\phi_{m'}(\mathbf{r}')|^2, \quad (\text{A1})$$

With this approach, we get  $U_{\text{bare}} = 1.99\text{eV}$  and  $V_{\text{bare}} = 235\text{meV}$ , giving a ratio  $U_{\text{bare}}/V_{\text{bare}} = 8.46$ . While these values might seems to be very large, we can compare them to the estimate we would get for a  $1s$  hydrogenic orbital of the form  $\phi_{1s}(\mathbf{r}) = \left(\frac{Z^3}{\pi}\right)^{1/2} e^{-Zr}$ , the on-site Coulomb integral  $\langle \phi_{1s} \phi_{1s} | v | \phi_{1s} \phi_{1s} \rangle = \frac{5}{8}Z$ . If we choose  $Z$  such that the spread of the Wannier function is the same as the spread of the Wannier state given by Wannier90 (here  $\approx 30\text{\AA}$ ), we obtain that  $Z \approx 0.25$ . This would lead to  $\langle \phi_{1s} \phi_{1s} | v | \phi_{1s} \phi_{1s} \rangle \approx 4.25\text{eV}$ .

We now proceed with estimating the screened Coulomb interaction. Key to the two-dimensional materials is the change of screening compare to three-dimensional materials. To take into account the two-dimensional nature of the material, we compute the screened Coulomb integrals for the twisted bilayer system, replacing the bare Coulomb potential by the Rytova-Keldysh potential[79, 80] which reads in real-space

$$V_{2D}(s) = \frac{\pi}{2\rho_0} \left[ H_0\left(\frac{s}{\rho_0}\right) - Y_0\left(\frac{s}{\rho_0}\right) \right], \quad (\text{A2})$$

TABLE II. **Tight-binding parameters of the moiré flat bands for  $90^\circ$  twisted multilayer GeX/SnX fitted to DFT bandstructures.**

| Materials                 | $t_x$ (meV) | $t_y$ (meV) | $t'_1$ (meV) | $t'_2$ (meV) |
|---------------------------|-------------|-------------|--------------|--------------|
| 2L-GeS                    | -6.054      | -6.054      | 0.271        | 0.271        |
| 2L-SnS                    | -0.410      | -0.410      | -0.015       | -0.015       |
| 2L-GeSe                   | -0.185      | -0.185      | -0.019       | -0.019       |
| 2L-GeSe (0.1)*            | -0.209      | -0.169      | -0.023       | -0.017       |
| 2L-GeSe (0.2)*            | -0.240      | -0.159      | -0.028       | -0.016       |
| 2L-GeSe (0.3)*            | -0.279      | -0.155      | -0.032       | -0.022       |
| 3L-GeSe                   | -0.481      | 0.527       | -0.010       | -0.040       |
| 4L (III-I)-GeSe           | -0.947      | 0.967       | -0.010       | -0.081       |
| 4L (II-II (AB-A'B'))-GeSe | 0.188       | 0.172       | -0.050       | -0.028       |
| 4L (II-II (AB-B'A'))-GeSe | 0.199       | 0.199       | -0.038       | -0.038       |

\* The asterisk denotes results with external electric field. The value of the applied field is indicated in the parentheses with unit of  $\text{eV/\AA}$ .

where  $H_0$  and  $Y_0$  are respectively the Struve and Bessel functions of the second kind and  $\rho_0$  is a screening length, which is obtained here *ab initio* from a calculation for the untwisted bilayer calculation as explained above. In Fourier space, this potential reads

$$V_{2D}(\mathbf{q}_{\parallel}) = \frac{2\pi}{|\mathbf{q}_{\parallel}|(1 + \rho_0|\mathbf{q}_{\parallel}|)}, \quad (\text{A3})$$

ad properly captures the asymptotic behavior of the two-dimensional screening [81]. In order to determine the screening length  $\rho_0 = \frac{d\epsilon}{2}$ , we use a method originally proposed by Qiu et al. [82] which consists in computing an effective *ab initio* screening from calculations done in a supercell

$$\epsilon_{2D}^{-1}(q) = \frac{q}{2\pi L_z} \sum_{\mathbf{G}_z, \mathbf{G}'_z} W_{\mathbf{G}_z, \mathbf{G}'_z}(q), \quad (\text{A4})$$

where  $W_{\mathbf{G}_z, \mathbf{G}'_z}(q)$  is the usual screened Coulomb interaction, computed using the Coulomb truncation technique, as suggested in Ref. [82]. The calculation of the screened Coulomb interaction  $W_{\mathbf{G}_z, \mathbf{G}'_z}(q)$  was performed using the Abinit code for the untwisted, fully-relaxed, bilayer system. We used a dense  $32 \times 32$  k-point grid, a supercell size  $L_z = 24\text{\AA}$ , with a cutoff energy of 13 Ha for the screening, and using 500 bands for computing the dielectric function. With this, we obtained an effective thickness  $d = 35\text{\AA}$  which is a bit less than four times the atom-to-atom distance for the bilayer system, with the experimental value of  $\epsilon = 13.6$ . This value was then used to evaluate the potential  $V_{2D}(\mathbf{q}_{\parallel})$  in evaluating the effective  $U$  and  $V$  for the twisted bilayer system.

In order to evaluate the Rytova-Keldysh potential with FFTs for the non-periodic Wannier orbitals, one resort to a Coulomb integral technique. This implies to compute the Fourier transform of  $V_{2D}(s)$  on a sphere of finite radius  $R$ . The analytical solution for the vanishing in-plane momentum  $\mathbf{G}_{\parallel} = 0$  is given by  $V_{2D}^{\text{cutoff}}(\mathbf{G}_{\parallel} = 0) = \pi^2 \rho_0 \left[ \frac{R}{\rho_0} \left( H_1\left(\frac{R}{\rho_0}\right) - Y_1\left(\frac{R}{\rho_0}\right) \right) - \frac{2}{\pi} \right] \approx 2\pi R^2 \frac{[1 - 2\gamma - 2\log(\frac{R}{2\rho_0})]}{4\rho_0}$ , where  $\gamma$  is the Euler-Mascheroni constant. The last expression is obtained using the fact that  $R \ll \rho_0$  in the present work.

Using the above expressions, we obtained  $U = 1.448\text{meV}$  and  $V = 0.145\text{meV}$ , leading to a ratio  $U/V \sim 9.99$ .

- 
- [1] J. Hubbard, Electron correlations in narrow energy bands, Proc. R. Soc. Lond. A **276**, 238– (1963).
- [2] J. Kanamori, Electron Correlation and Ferromagnetism of Transition Metals, Progress of Theoretical Physics **30**, 275 (1963).
- [3] M. C. Gutzwiller, Effect of correlation on the ferromagnetism of transition metals, Phys. Rev. Lett. **10**, 159 (1963).
- [4] E. Manousakis, The spin- $\frac{1}{2}$  heisenberg antiferromagnet on a square lattice and its application to the cuprous oxides, Rev. Mod. Phys. **63**, 1 (1991).
- [5] P. W. Anderson, The resonating valence bond state in  $\text{La}_2\text{CuO}_4$  and superconductivity, Science **235**, 1196 (1987).
- [6] V. J. Emery, Theory of high- $T_c$  superconductivity in oxides, Phys. Rev. Lett. **58**, 2794 (1987).
- [7] B.-X. Zheng, C.-M. Chung, P. Corboz, G. Ehlers, M.-P. Qin, R. M. Noack, H. Shi, S. R. White, S. Zhang, and G. K.-L. Chan, Stripe order in the underdoped region of the two-dimensional hubbard model, Science **358**, 1155 (2017).
- [8] E. W. Huang, C. B. Mendl, H.-C. Jiang, B. Moritz, and T. P. Devereaux, Stripe order from the perspective of the hubbard model, npj Quantum Materials **3**, 22 (2018).
- [9] P. W. Phillips, N. E. Hussey, and P. Abbamonte, Stranger than metals, Science **377**, eabh4273 (2022).
- [10] T. Timusk and B. Statt, The pseudogap in high-temperature superconductors: an experimental survey, Reports on Progress in Physics **62**, 61 (1999).
- [11] M. Qin, T. Schäfer, S. Andergassen, P. Corboz, and E. Gull, The hubbard model: A computational perspective, Annual Review of Condensed Matter Physics **13**, 275 (2022).
- [12] E. Dagotto, Correlated electrons in high-temperature superconductors, Rev. Mod. Phys. **66**, 763 (1994).
- [13] P. A. Lee, N. Nagaosa, and X.-G. Wen, Doping a mott insulator: Physics of high-temperature superconductivity, Rev. Mod. Phys. **78**, 17 (2006).
- [14] D. P. Arovas, E. Berg, S. A. Kivelson, and S. Raghu, The hubbard model, Annual Review of Condensed Matter Physics **13**, 239 (2022).
- [15] J. P. F. LeBlanc, A. E. Antipov, F. Becca, I. W. Bulik, G. K.-L. Chan, C.-M. Chung, Y. Deng, M. Ferrero, T. M. Henderson, C. A. Jiménez-Hoyos, E. Kozik, X.-W. Liu, A. J. Millis, N. V. Prokof'ev, M. Qin, G. E. Scuseria, H. Shi, B. V. Svistunov, L. F. Tocchio, I. S. Tupitsyn, S. R. White, S. Zhang, B.-X. Zheng, Z. Zhu, and E. Gull (Simons Collaboration on the Many-Electron Problem), Solutions of the two-dimensional hubbard model: Benchmarks and results from a wide range of numerical algorithms, Phys. Rev. X **5**, 041041 (2015).
- [16] S. R. White, Density matrix formulation for quantum renormalization groups, Phys. Rev. Lett. **69**, 2863 (1992).
- [17] S. R. White, Density-matrix algorithms for quantum renormalization groups, Phys. Rev. B **48**, 10345 (1993).
- [18] A. Georges, G. Kotliar, W. Krauth, and M. J. Rozenberg, Dynamical mean-field theory of strongly correlated fermion systems and the limit of infinite dimensions, Rev. Mod. Phys. **68**, 13 (1996).
- [19] J. E. Hirsch, Two-dimensional hubbard model: Numerical simulation study, Phys. Rev. B **31**, 4403 (1985).
- [20] S. R. White, D. J. Scalapino, R. L. Sugar, E. Y. Loh, J. E. Gubernatis, and R. T. Scalettar, Numerical study of the two-dimensional hubbard model, Phys. Rev. B **40**, 506 (1989).
- [21] M. Qin, H. Shi, and S. Zhang, Benchmark study of the two-dimensional hubbard model with auxiliary-field quantum monte carlo method, Phys. Rev. B **94**, 085103 (2016).
- [22] T. Maier, M. Jarrell, T. Pruschke, and M. H. Hettler, Quantum cluster theories, Rev. Mod. Phys. **77**, 1027 (2005).
- [23] H.-C. Jiang and T. P. Devereaux, Superconductivity in the doped hubbard model and its interplay with next-nearest hopping  $t'$ , Science **365**, 1424 (2019).
- [24] R. Jördens, N. Strohmaier, K. Günter, H. Moritz, and T. Esslinger, A mott insulator of fermionic atoms in an optical lattice, Nature **455**, 204 (2008).
- [25] R. A. Hart, P. M. Duarte, T.-L. Yang, X. Liu, T. Paiva, E. Khatami, R. T. Scalettar, N. Trivedi, D. A. Huse, and R. G. Hulet, Observation of antiferromagnetic correlations in the hubbard model with ultracold atoms, Nature **519**, 211 (2015).
- [26] A. Mazurenko, C. S. Chiu, G. Ji, M. F. Parsons, M. Kanász-Nagy, R. Schmidt, F. Grusdt, E. Demler, D. Greif, and M. Greiner, A cold-atom fermi-hubbard antiferromagnet, Nature **545**, 462 (2017).
- [27] C. Gross and I. Bloch, Quantum simulations with ultracold atoms in optical lattices, Science **357**, 995 (2017).
- [28] A. Singha, M. Gibertini, B. Karmakar, S. Yuan, M. Polini, G. Vignale, M. Katsnelson, A. Pinczuk, L. Pfeiffer, K. West, *et al.*, Two-dimensional mott-hubbard electrons in an artificial honeycomb lattice, Science **332**, 1176 (2011).
- [29] T. Hensgens, T. Fujita, L. Janssen, X. Li, C. Van Diepen, C. Reichl, W. Wegscheider, S. Das Sarma, and L. M. Vandersypen, Quantum simulation of a fermi-hubbard model using a semiconductor quantum dot array, Nature **548**, 70 (2017).
- [30] D. Wecker, M. B. Hastings, N. Wiebe, B. K. Clark, C. Nayak, and M. Troyer, Solving strongly correlated electron models on a quantum computer, Phys. Rev. A **92**, 062318 (2015).
- [31] S. Stanisic, J. L. Bosse, F. M. Gambetta, R. A. Santos, W. Mruczkiewicz, T. E. O'Brien, E. Ostby, and A. Montanaro, Observing ground-state properties of the fermi-hubbard model using a scalable algorithm on a quantum computer, Nature Communications **13**, 5743 (2022).
- [32] M. Xu, L. H. Kendrick, A. Kale, Y. Gang, G. Ji, R. T. Scalettar, M. Lebrat, and M. Greiner, Frustration-and doping-induced magnetism in a fermi-hubbard simulator, Nature **620**, 971 (2023).
- [33] K. Novoselov, A. Mishchenko, A. Carvalho, and A. Castro Neto, 2d materials and van der waals heterostructures, Science **353**, aac9439 (2016).
- [34] M. C. Lemme, D. Akinwande, C. Huyghebaert, and C. Stampfer, 2d materials for future heterogeneous electronics, Nature communications **13**, 1392 (2022).
- [35] P. Ares and K. S. Novoselov, Recent advances in graphene and other 2d materials, Nano Materials Science **4**, 3 (2022).
- [36] S. H. Choi, S. J. Yun, Y. S. Won, C. S. Oh, S. M. Kim, K. K. Kim, and Y. H. Lee, Large-scale synthesis of graphene and other 2d materials towards industrialization, Nature Communications **13**, 1484 (2022).
- [37] A. Castellanos-Gomez, X. Duan, Z. Fei, H. R. Gutierrez, Y. Huang, X. Huang, J. Queda, Q. Qian, E. Sutter, and P. Sutter, Van der waals heterostructures, Nature Reviews Methods Primers **2**, 58 (2022).
- [38] Y. Cao, V. Fatemi, S. Fang, K. Watanabe, T. Taniguchi, E. Kaxi-



- ras, and P. Jarillo-Herrero, Unconventional superconductivity in magic-angle graphene superlattices, *Nature* **556**, 43 (2018).
- [39] Y. Cao, V. Fatemi, A. Demir, S. Fang, S. L. Tomarken, J. Y. Luo, J. D. Sanchez-Yamagishi, K. Watanabe, T. Taniguchi, E. Kaxiras, *et al.*, Correlated insulator behaviour at half-filling in magic-angle graphene superlattices, *Nature* **556**, 80 (2018).
- [40] Y. Choi, J. Kemmer, Y. Peng, A. Thomson, H. Arora, R. Polski, Y. Zhang, H. Ren, J. Alicea, G. Refael, *et al.*, Electronic correlations in twisted bilayer graphene near the magic angle, *Nature physics* **15**, 1174 (2019).
- [41] A. Kerelsky, L. J. McGilly, D. M. Kennes, L. Xian, M. Yankowitz, S. Chen, K. Watanabe, T. Taniguchi, J. Hone, C. Dean, *et al.*, Maximized electron interactions at the magic angle in twisted bilayer graphene, *Nature* **572**, 95 (2019).
- [42] E. Y. Andrei and A. H. MacDonald, Graphene bilayers with a twist, *Nature materials* **19**, 1265 (2020).
- [43] L. Wang, E.-M. Shih, A. Ghiotto, L. Xian, D. A. Rhodes, C. Tan, M. Claassen, D. M. Kennes, Y. Bai, B. Kim, *et al.*, Correlated electronic phases in twisted bilayer transition metal dichalcogenides, *Nature materials* **19**, 861 (2020).
- [44] Y. Xu, S. Liu, D. A. Rhodes, K. Watanabe, T. Taniguchi, J. Hone, V. Elser, K. F. Mak, and J. Shan, Correlated insulating states at fractional fillings of moiré superlattices, *Nature* **587**, 214 (2020).
- [45] K. F. Mak and J. Shan, Semiconductor moiré materials, *Nature Nanotechnology* **17**, 686 (2022).
- [46] Y. Zeng, Z. Xia, K. Kang, J. Zhu, P. Knüppel, C. Vaswani, K. Watanabe, T. Taniguchi, K. F. Mak, and J. Shan, Thermodynamic evidence of fractional chern insulator in moiré mote2, *Nature* **622**, 69 (2023).
- [47] H. Park, J. Cai, E. Anderson, Y. Zhang, J. Zhu, X. Liu, C. Wang, W. Holtzmann, C. Hu, Z. Liu, *et al.*, Observation of fractionally quantized anomalous hall effect, *Nature* **622**, 74 (2023).
- [48] F. Xu, Z. Sun, T. Jia, C. Liu, C. Xu, C. Li, Y. Gu, K. Watanabe, T. Taniguchi, B. Tong, *et al.*, Observation of integer and fractional quantum anomalous hall effects in twisted bilayer mote2, *Physical Review X* **13**, 031037 (2023).
- [49] R. Bistritzer and A. H. MacDonald, Moiré bands in twisted double-layer graphene, *Proceedings of the National Academy of Sciences* **108**, 12233 (2011).
- [50] F. Wu, T. Lovorn, E. Tutuc, and A. H. MacDonald, Hubbard model physics in transition metal dichalcogenide moiré bands, *Physical review letters* **121**, 026402 (2018).
- [51] Y. Tang, L. Li, T. Li, Y. Xu, S. Liu, K. Barmak, K. Watanabe, T. Taniguchi, A. H. MacDonald, J. Shan, *et al.*, Simulation of hubbard model physics in wse2/ws2 moiré superlattices, *Nature* **579**, 353 (2020).
- [52] L. Xian, M. Claassen, D. Kiese, M. M. Scherer, S. Trebst, D. M. Kennes, and A. Rubio, Realization of nearly dispersionless bands with strong orbital anisotropy from destructive interference in twisted bilayer mos2, *Nature communications* **12**, 5644 (2021).
- [53] D. M. Kennes, M. Claassen, L. Xian, A. Georges, A. J. Millis, J. Hone, C. R. Dean, D. N. Basov, A. N. Pasupathy, and A. Rubio, Moiré heterostructures as a condensed-matter quantum simulator, *Nat. Phys.* **17**, 155 (2021).
- [54] Y. Xu, K. Kang, K. Watanabe, T. Taniguchi, K. F. Mak, and J. Shan, A tunable bilayer hubbard model in twisted wse2, *Nature Nanotechnology* **17**, 934 (2022).
- [55] D. M. Kennes, L. Xian, M. Claassen, and A. Rubio, One-dimensional flat bands in twisted bilayer germanium selenide, *Nature communications* **11**, 1124 (2020).
- [56] P. Wang, G. Yu, Y. H. Kwan, Y. Jia, S. Lei, S. Klemenz, F. A. Cevallos, R. Singha, T. Devakul, K. Watanabe, *et al.*, One-dimensional luttinger liquids in a two-dimensional moiré lattice, *Nature* **605**, 57 (2022).
- [57] M. Claassen, L. Xian, D. M. Kennes, and A. Rubio, Ultrastrong spin-orbit coupling and topological moiré engineering in twisted zrs2 bilayers, *Nature communications* **13**, 4915 (2022).
- [58] K. Chang and S. S. Parkin, Experimental formation of monolayer group-iv monochalcogenides, *Journal of Applied Physics* **127**, 220902 (2020).
- [59] A. D. Oyedele, S. Yang, L. Liang, A. A. Puzos, K. Wang, J. Zhang, P. Yu, P. R. Pudasaini, A. W. Ghosh, Z. Liu, *et al.*, Pdse2: pentagonal two-dimensional layers with high air stability for electronics, *Journal of the American Chemical Society* **139**, 14090 (2017).
- [60] E. C. Regan, D. Wang, C. Jin, M. I. Bakti Utama, B. Gao, X. Wei, S. Zhao, W. Zhao, Z. Zhang, K. Yumigeta, *et al.*, Mott and generalized wigner crystal states in wse2/ws2 moiré superlattices, *Nature* **579**, 359 (2020).
- [61] C. N. Lau, M. W. Bockrath, K. F. Mak, and F. Zhang, Reproducibility in the fabrication and physics of moiré materials, *Nature* **602**, 41 (2022).
- [62] H. Wiedemeier, H. Georg, and G. von Schnering, Refinement of the structures of ges, gese, sns and snse, *Zeitschrift für Kristallographie-Crystalline Materials* **148**, 295 (1978).
- [63] C. N. Varney, C.-R. Lee, Z. J. Bai, S. Chiesa, M. Jarrell, and R. T. Scalettar, Quantum monte carlo study of the two-dimensional fermion hubbard model, *Phys. Rev. B* **80**, 075116 (2009).
- [64] D. F. Agterberg, J. S. Davis, S. D. Edkins, E. Fradkin, D. J. Van Harlingen, S. A. Kivelson, P. A. Lee, L. Radzihovsky, J. M. Tranquada, and Y. Wang, The physics of pair-density waves: Cuprate superconductors and beyond, *Annual Review of Condensed Matter Physics* **11**, 231 (2020).
- [65] E. Berg, E. Fradkin, E.-A. Kim, S. A. Kivelson, V. Oganesyan, J. M. Tranquada, and S. C. Zhang, Dynamical layer decoupling in a stripe-ordered high- $T_c$  superconductor, *Phys. Rev. Lett.* **99**, 127003 (2007).
- [66] P. A. Lee, Amperean pairing and the pseudogap phase of cuprate superconductors, *Phys. Rev. X* **4**, 031017 (2014).
- [67] K. Ido, T. Ohgoe, and M. Imada, Competition among various charge-inhomogeneous states and  $d$ -wave superconducting state in hubbard models on square lattices, *Phys. Rev. B* **97**, 045138 (2018).
- [68] L. F. Tocchio, A. Montorsi, and F. Becca, Metallic and insulating stripes and their relation with superconductivity in the doped hubbard model, *SciPost Phys.* **7**, 021 (2019).
- [69] A. S. Darmawan, Y. Nomura, Y. Yamaji, and M. Imada, Stripe and superconducting order competing in the hubbard model on a square lattice studied by a combined variational monte carlo and tensor network method, *Phys. Rev. B* **98**, 205132 (2018).
- [70] B. Ponsioen, S. S. Chung, and P. Corboz, Period 4 stripe in the extended two-dimensional hubbard model, *Phys. Rev. B* **100**, 195141 (2019).
- [71] G. Kresse and J. Furthmüller, Efficient iterative schemes for ab initio total-energy calculations using a plane-wave basis set, *Physical review B* **54**, 11169 (1996).
- [72] P. E. Blöchl, Projector augmented-wave method, *Physical review B* **50**, 17953 (1994).
- [73] J. P. Perdew, K. Burke, and M. Ernzerhof, Generalized gradient approximation made simple, *Physical review letters* **77**, 3865 (1996).
- [74] A. Tkatchenko and M. Scheffler, Accurate molecular van der waals interactions from ground-state electron density and free-atom reference data, *Physical review letters* **102**, 073005 (2009).

- [75] N. Tancogne-Dejean, M. J. Oliveira, X. Andrade, H. Appel, C. H. Borca, G. Le Breton, F. Buchholz, A. Castro, S. Corni, A. A. Correa, *et al.*, Octopus, a computational framework for exploring light-driven phenomena and quantum dynamics in extended and finite systems, *The Journal of chemical physics* **152**, 124119 (2020).
- [76] N. Tancogne-Dejean, M. J. T. Oliveira, and A. Rubio, Self-consistent DFT +  $u$  method for real-space time-dependent density functional theory calculations, *Phys. Rev. B* **96**, 245133 (2017).
- [77] C. Hartwigsen, S. Goedecker, and J. Hutter, Relativistic separable dual-space gaussian pseudopotentials from h to rn, *Phys. Rev. B* **58**, 3641 (1998).
- [78] G. Pizzi, V. Vitale, R. Arita, S. Blügel, F. Freimuth, G. Géranton, M. Gibertini, D. Gresch, C. Johnson, T. Koretsune, J. Ibañez-Azpiroz, H. Lee, J.-M. Lihm, D. Marchand, A. Marrazzo, Y. Mokrousov, J. I. Mustafa, Y. Nohara, Y. Nomura, L. Paulatto, S. Poncé, T. Ponweiser, J. Qiao, F. Thöle, S. S. Tsirkin, M. Wierzbowska, N. Marzari, D. Vanderbilt, I. Souza, A. A. Mostofi, and J. R. Yates, Wannier90 as a community code: new features and applications, *Journal of Physics: Condensed Matter* **32**, 165902 (2020).
- [79] N. S. Rytova, Screened potential of a point charge in a thin film, arXiv preprint arXiv:1806.00976 (2018).
- [80] L. Keldysh, Coulomb interaction in thin semiconductor and semimetal films, in *SELECTED PAPERS OF LEONID V KELDYSH* (World Scientific, 2024) pp. 155–158.
- [81] P. Cudazzo, I. V. Tokatly, and A. Rubio, Dielectric screening in two-dimensional insulators: Implications for excitonic and impurity states in graphane, *Phys. Rev. B* **84**, 085406 (2011).
- [82] D. Y. Qiu, F. H. da Jornada, and S. G. Louie, Screening and many-body effects in two-dimensional crystals: Monolayer  $\text{mos}_2$ , *Phys. Rev. B* **93**, 235435 (2016).
- [83] K. Góral, L. Santos, and M. Lewenstein, Quantum phases of dipolar bosons in optical lattices, *Phys. Rev. Lett.* **88**, 170406 (2002).
- [84] D. Jaksch and P. Zoller, The cold atom hubbard toolbox, *Annals of Physics* **315**, 52 (2005), special Issue.
- [85] M. Greiner, O. Mandel, T. Esslinger, T. W. Hänsch, and I. Bloch, Quantum phase transition from a superfluid to a mott insulator in a gas of ultracold atoms, *Nature* **415**, 39 (2002).
- [86] J. Hubbard, Electron correlations in narrow energy bands. ii. the degenerate band case, *Proceedings of the Royal Society of London. Series A. Mathematical and Physical Sciences* **277**, 237 (1964).
- [87] N. Tancogne-Dejean and A. Rubio, Parameter-free hybridlike functional based on an extended hubbard model: DFT +  $u + v$ , *Phys. Rev. B* **102**, 155117 (2020).
- [88] C. M. Varma, Colloquium: Linear in temperature resistivity and associated mysteries including high temperature superconductivity, *Rev. Mod. Phys.* **92**, 031001 (2020).
- [89] D. Jaksch and P. Zoller, The cold atom hubbard toolbox, *Annals of physics* **315**, 52 (2005).
- [90] C. Wang, L. You, D. Cobden, and J. Wang, Towards two-dimensional van der waals ferroelectrics, *Nature Materials*, 1 (2023).
- [91] Y. Wu, D. Li, C.-L. Wu, H. Y. Hwang, and Y. Cui, Electrostatic gating and intercalation in 2d materials, *Nature Reviews Materials* **8**, 41 (2023).
- [92] J. M. Park, Y. Cao, K. Watanabe, T. Taniguchi, and P. Jarillo-Herrero, Tunable strongly coupled superconductivity in magic-angle twisted trilayer graphene, *Nature* **590**, 249 (2021).
- [93] H. Kim, Y. Choi, C. Lewandowski, A. Thomson, Y. Zhang, R. Polski, K. Watanabe, T. Taniguchi, J. Alicea, and S. Nadj-Perge, Evidence for unconventional superconductivity in twisted trilayer graphene, *Nature* **606**, 494 (2022).
- [94] A. Inbar, J. Birkbeck, J. Xiao, T. Taniguchi, K. Watanabe, B. Yan, Y. Oreg, A. Stern, E. Berg, and S. Ilani, The quantum twisting microscope, *Nature* **614**, 682 (2023).
- [95] S. Carr, S. Fang, and E. Kaxiras, Electronic-structure methods for twisted moiré layers, *Nature Reviews Materials* **5**, 748 (2020).
- [96] H. Pan, F. Wu, and S. D. Sarma, Quantum phase diagram of a moiré-hubbard model, *Physical Review B* **102**, 201104 (2020).